JOURNAL OF SYNCHROTRON RADIATION

ISSN 1600-5775

Received 2 March 2017
Accepted 27 June 2017

Edited by S. M. Heald, Argonne National Laboratory, USA

Keywords: Flyscan method; theranostic vectors; gold-cluster-enriched mesoporous silica nanospheres; X-ray fluorescence; XANES.

Flyscan opportunities in medicine: the case of quantum rattle based on gold quantum dots

Emmanuel Esteve,[a,b] Solenn Reguer,[c] Cédric Boissiere,[b] Corinne Chanéac,[b] Gustavo Lugo,[b,d] Chantal Jouanneau,[a] Cristian Mocuta,[c] Dominique Thiaudière,[c] Nicolas Leclercq,[c] Bernard Leyh,[d] Jean-François Greisch,[e] Julien Berthault,[c] Michel Daudon,[a,f] Pierre Ronco[a,f] and Dominique Bazin[b]*

[a]UMR S1155, INSERM/UPMC, 4 Rue de la Chine, 75970 Paris Cedex 20, France, [b]Laboratoire Chimie de la Matière Condensée de Paris, UMR UPMC College de France – CNRS 7574, Université Pierre et Marie Curie (Paris 6), 4 Place Jussieu, 75252 Paris, France, [c]Synchrotron SOLEIL, L'Orme des Merisiers, Saint-Aubin, BP 48, 91192 Gif-sur-Yvette, France, [d]Department of Chemistry, University of Liège, B4000 Liège, Belgium, [e]Karlsruhe Institute of Technology, Institute of Nanotechnology, Hermann-von-Helmholtz-Platz 1, 76344 Eggenstein-Leopoldshafen, Germany, and [f]AP-HP, Hôpital Tenon, 4 Rue de la Chine, 75970 Paris Cedex 20, France.
*Correspondence e-mail: dominique.bazin@upmc.fr

The new rapid scan method, Flyscan mode, implemented on the DiffAbs beamline at Synchrotron SOLEIL, allows fast micro-X-ray fluorescence data acquisition. It paves the way for applications in the biomedical field where a large amount of data is needed to generate meaningful information for the clinician. This study presents a complete set of data acquired after injection of gold-cluster-enriched mesoporous silica nanospheres, used as potential theranostic vectors, into rats. While classical X-ray fluorescence investigations (using step-by-step acquisitions) are based on a limited number of samples (approximately one per day at the DiffAbs beamline), the Flyscan mode has enabled gathering information on the interaction of nanometer-scale vectors in different organs such as liver, spleen and kidney at the micrometer scale, for five rats, in only a single five-day synchrotron shift. Moreover, numerous X-ray absorption near-edge structure spectra, which are beam-time-consuming taking into account the low concentration of these theranostic vectors, were collected.

1. Introduction

Nanometer-scale systems for the treatment of different severe pathologies including cancer promise to improve prognosis through a synergic combination of diagnosis and therapy, thereby facilitating personalized medicine (Min *et al.*, 2015; Nguyen & Zhao, 2015). The avalanche of new publications dedicated to such research has focused on two kinds of materials, namely mesoporous silica (Slowing *et al.*, 2007; Yuan *et al.*, 2016) and gold nanostructures (Yang *et al.*, 2015), as advanced materials to enhance treatment.

However, although gold nanostructures of less than 2 nm [gold quantum dots (AuQDs)] could be transformative for live imaging, they have rarely been used *in vivo*, due to limited efficacy. Recently, new materials called 'quantum rattles' (QRs) based on AuQDs (<2 nm) and gold nanoparticles of 7 nm (AuNPs) confined in mesoporous silica were proposed to improve prognosis *via* a single multifunctional agent (Hembury *et al.*, 2015). These AuQDs absorb light in the near-infrared (NIR) biological window (650–900 nm) (Jain *et al.*, 2008) and convert it into photons and heat (Shang *et al.*, 2011). Thus, the presence of Au clusters can be used to visualize the spatial distribution through NIR spectroscopy. Although their properties are well defined and their *in vitro* cytotoxicity is

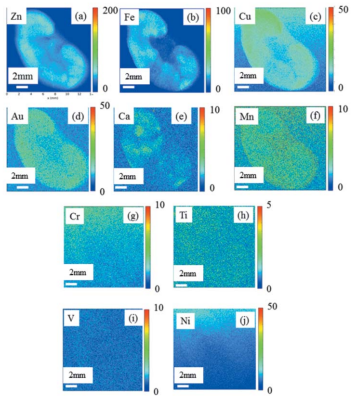

very moderate, very little is known about their *in vivo* toxicity. To attain this goal, information regarding their partitioning into different organs is essential.

In the present paper, X-ray fluorescence spectroscopy (XRF) has been used to investigate the spatial distribution of QR-AuQDs in various rat organs, employing a novel recently developed experimental approach, Flyscan (Leclercq *et al.*, 2015). To illustrate the possibilities and utility of Flyscan implemented on the DiffAbs beamline (Synchrotron SOLEIL), results obtained from medical nanomaterials used as potential dedicated theranostic vectors are presented. More specifically, micro-XRF (μXRF) spectroscopy is used to precisely describe the spatial repartitioning of QR-AuQDs in diverse rat organs and micro-X-ray absorption spectroscopy (μXAS) to interrogate possible structural modifications of AuQDs. The complete set of data across several animals will help the clinician to investigate the interaction between nanosystems and biological tissues (liver, spleen and kidney) more thoroughly, leading to the development of more efficient drugs.

2. Material and methods

2.1. Sample collection and preparation

Highly monodisperse 100 nm-diameter mesoporous silica nanospheres were produced according to the standard Stöber procedure (Stöber *et al.*, 1968). They were then covered by a thin layer of polyethyleneglycol (PEG) to improve biocompatibility by letting 10 mg PEG silane react with 150 mg of silica spheres overnight at room temperature. Synthesis of an Au_{25} cluster with 4-aminothiophenol (4ATP) as ligand was achieved using the technique developed by Lavenn *et al.* (2012). Two solutions, one containing 4 eq. of reducing agent ($LiBH_4$) dissolved in tetrahydrofuran (thf, 25 ml), the other 1 eq. of gold (III) chloride trihydrate ($HAuCl_4{\cdot}3H_2O$) in thf (25 ml), were slowly introduced into 20 ml of thf with 2 eq. 4ATP at a rate of 60 ml h^{-1}, at 4°C (ice bath). After 5 h of stirring at 500 r.p.m., keeping the temperature at less than 25°C, a black precipitate was formed. The thf was removed using a rotavapor at 40°C and 300 mbar. Next, the black solid was washed three times with ethanol and centrifuged at 8000 r.p.m. for 15 min. Finally, the solid was dried in air. Resulting Au_{25} (4ATP) clusters were characterized by IR and UV–Vis spectroscopy, transmission electron microscopy (TEM), small-angle X-ray scattering, and by electrospray-ionization mass spectrometry (ESI-MS).

Fig. 1 shows the ESI-MS spectrum of the $[Au_{25}(ATP)_{18}]^-$ clusters acquired in negative mode by dissolving the nanoclusters in dimethyl sulfoxide (DMSO) to a final concentration of 1 mg ml^{-1}. The negative-ion mass spectrum is dominated by two peaks with high intensity, the first one near m/z = 7160 which corresponds to the $Au_{25}(4ATP)_{18}$ cluster and the second one around m/z = 3600 which corresponds to a doubly charged Au_{25} cluster with some of its ligands further reacted (corrupted). This result is in accordance with the average particle diameter (1.2 ± 0.3 nm) deduced from the TEM image (Fig. 1) on which small black points, corresponding to Au clusters, are visible inside large silica spheres of 100 nm.

To obtain theranostic vectors, gold clusters were added to the mesoporous silica sphere solution and stirred overnight in water at room temperature. The QR-AuQDs solid was washed with water three times using sequential centrifugation and ultrasonic dispersion.

Rats, 200 g Sprague Dawley, were injected intravenously with either saline solution or 10 mg of the therapeutic vector diluted in phosphate buffered saline (Euromedex France) to ensure physiological pH and tonicity; and sacrificed 2 h later. Liver, kidney and spleen were sampled, and fixed for 24 h in 1% acetic acid/ethanol 70°/10% formalin. Dehydration was performed in a carousel (Microm France STP MM 120) before paraffin (Leica/Paraplast Surgipath) embedding.

Intravenous injection was performed under isoflurane anesthesia (3.5% induction, 1.5% retention) to reduce stress and pain. The animals were housed under similar conditions (two rats per cage) with a 12 h dark/light cycle and fed *ad libitum* on standard rat chow. Environmental enrichment was routinely performed. All animal procedures were performed in accordance with the European Union Guidelines for the Care and Use of Laboratory Animals and this protocol was endorsed by our local Institutional Animal Care and Use Committees ('Comité d'éthique en experimentation

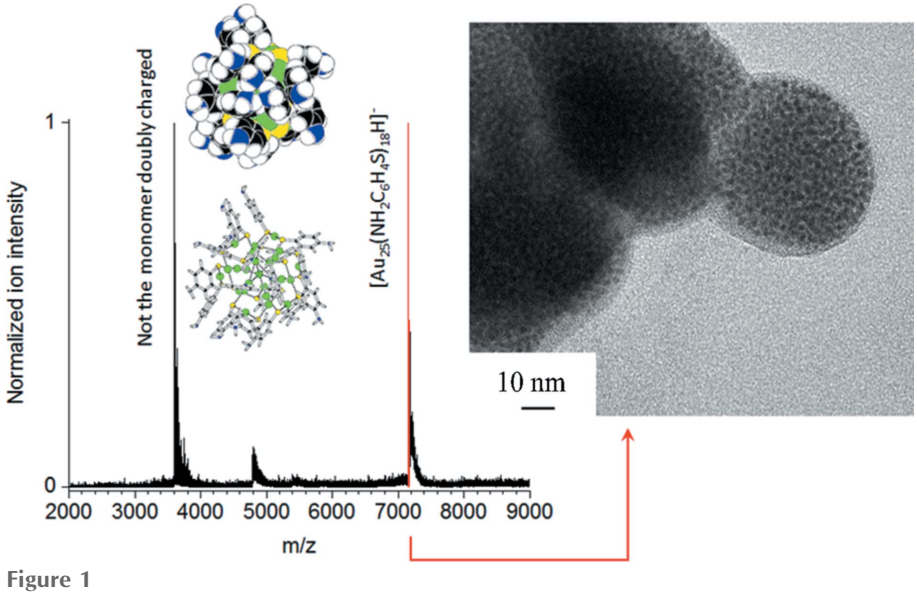

Figure 1
ESI mass and TEM image of the $Au_{25}(4ATP)_{18}$ clusters. The ESI-MS data spectrum was measured using a SYNAPT G2S-HDMS mass spectrometer equipped with an electrospray ionization source and TEM characterization was carried out using a FEI Tecnai G2 Spirit instrument operating on an acceleration tension of 120 kV. Clusters are dispersed in DMSO for analysis.

Charles Darwin C2EA-05'). Animals were anesthetized with a lethal intraperitoneal pentobarbital injection to minimize suffering before sacrifice.

2.2. Synchrotron μX-ray fluorescence and absorption spectroscopies

All experiments were performed at room temperature and atmospheric pressure on the DiffAbs beamline (Reguer *et al.*, 2016) at the SOLEIL synchrotron facility (France). On this beamline the Si(111) double-crystal monochromator is positioned between two cylindrical vertically focusing mirrors in order to monochromatize and focus the beam to about 300 μm diameter. An additional microbeam set-up consisting of two trapezoidal orthogonally positioned curved mirrors under grazing incidence (Kirkpatrick-Baez geometry; Kirkpatrick & Baez, 1948) allows the X-ray beam to be focused to a ∼5 μm-diameter beam spot.

The DiffAbs beamline offers powerful tools for multi-technique and multi-scale characterization of various materials (Nguyen *et al.*, 2011). Indeed, combination of μXRF and X-ray absorption spectroscopies [micro-X-ray absorption near-edge structure (μXANES) and micro-extended X-ray absorption fine structure (μEXAFS) (Sayers *et al.*, 1971), as well as X-ray diffraction (XRD), can yield morphological, chemical and structural information. Such techniques can be applied in local probe, or imaging (raster maps), modes to highlight localization and distribution of both chemical elements and structured phases (Dessombz *et al.*, 2013).

All previous samples were analyzed by μXRF and μXAS using the microbeam setup with a beam spot of ∼9 μm × 7 μm [horizontal × vertical, full width at half-maximum (FWHM)]. The acquisition and data treatment methodology are described hereafter.

2.2.1. μXRF measurements using new Flyscan development. The Flyscan mode (Leclercq *et al.*, 2015), the availability of fast reading and highly efficient detectors, as well as an intense (large photon flux) focused X-ray beam make it possible to acquire data points with frequencies of up to several hundreds of Hz. Mapping of several 10 mm^2 with a lateral resolution of about 10 μm can be rapidly performed (intervals of time less than 1 h) with absorption, fluorescence and/or diffusion (diffraction) contrasts (Mocuta *et al.*, 2014), since the measurement overhead, in addition to the measurement time, amounts to a few seconds per scanned line (*i.e.* up to a few milliseconds per datapoint only, a line in the map consisting of ∼1000 points). This means that it does not act as a coarse scanning solution requiring a complementary step-by-step scan to be performed on a different region of the sample. The data delivered by the involved sensors, *i.e.* one-dimensional and/or two-dimensional detectors, are obtained in a single pass. Motor positions are hardware sampled at each point of the scan space using the master clock (*i.e.* trigger) shared by the scan actors. Moreover, the master clock pattern can be itself generated by the motor position (*e.g.* one trigger pulse every micrometer). Recording the actuator position allows position reproducibility or velocity regulation errors to be easily dealt with. The *in situ* data processing and visualization system is able to perform live data interpolation and normalization in order to provide the user with pre-treated images while the acquisition is in progress. On the sensors side, the system supports an unlimited number of 0, 1 and 2D data sources. For large scans, typically 1000 pixels × 1000 pixels, the data can be spread over several files in order to ease their post-acquisition treatment.

An XRF spectrum showing the different contributions from all chemical elements in a sample (but also in the sample holder and environment, *e.g.* Ar *K* lines from ambient air) is exemplified in Fig. 2. The experimental setup does not include a controlled atmosphere around the sample, thus Ar is obviously present in the air and will not be further discussed.

Analysis of the μXRF spectra was performed using the *pyMCA* software suite (Solé *et al.*, 2007). Energy calibration and a fitting procedure of the fluorescence lines for each spectrum allowed us to identify and evaluate the contribution of each element semi-quantitatively. μXRF maps of the elements identified correspond to the calculated area of the main Gaussian-fitted fluorescence lineshapes. Our therapeutical vector consists of silica and Au. Silica X-ray fluorescence cannot be detected using this configuration (the XRF energy corresponding to Si K_α at 1.74 keV is too low, due to the experimental condition in air) but the Au L_α signal can be exploited. The Gaussian lineshape model isolates Au L_α using narrow peaks of FWHM (region of interest) of 100 eV to remove the Zn K_β contribution. Thus the spatial distribution of Au, *i.e.* our theranostic vector, in the paraffin embedded samples can be mapped.

The methodology is as follows:

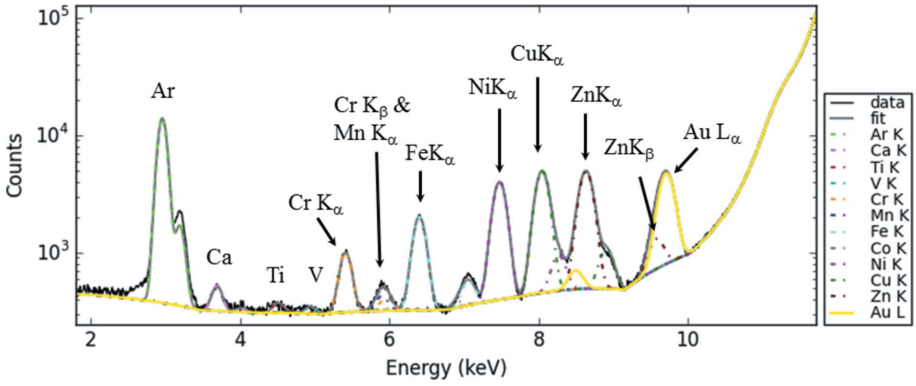

Figure 2
Typical X-ray fluorescence spectrum collected for a biological sample with the contribution of Ca (K_α at 3.691 keV, K_β at 4.012 keV), Fe (K_α at 6.404 keV, K_β at 7.058 keV), Zn (K_α at 8.638 keV, K_β at 9.572 keV). Special attention has been devoted to distinguish, by peak deconvolution, the respective contributions of Zn (K_β = 9.572 keV) and Au (L_α = 9.713 keV) in the region of interest between 9 and 10 keV.

(i) Firstly, large preliminary maps are collected for the different organs with spatial resolution of 500 µm (or less when possible) and acquisition time from 30 ms to 50 ms. This map shows chemical element distributions over the whole organ and allows a region of interest to be defined.

(ii) Secondly, more precise maps are acquired in the region of interest with spatial resolution from 10 µm to 30 µm, with 30 ms (or more) acquisition time.

As an example, Fig. 3 illustrates these two steps, with a large map and a resultant region of interest.

2.2.2. µXANES measurements. To further ensure the specificity of the Au signal and to explore the metabolism of the QR-AuQDs nanovectors the present experiment took advantage of the possibility of acquiring XANES spectra on the DiffAbs beamline. XANES spectra at the Au L_{III}-absorption edge (first inflection point in the absorption spectrum at 11.919 keV) were collected from 11.9 to 12.0 keV, with energy steps of 0.5 eV and a 3 s dwell time per point. The DiffAbs beamline monochromator provides the energy resolution of $\Delta E/E = 10^{-4}$ necessary for XANES measurements. Details regarding the experiments have appeared in previous publications on biological tissues including cartilage, kidney and bones (Carpentier *et al.*, 2010; Bazin *et al.*, 2011).

The Au distribution 'hot spots' (Fig. 4) are then selected and XANES spectra collected, allowing us to check the stability as well as the possible oxidation of the Au component of the theranostic vector (Song *et al.*, 2012). More precisely, as discussed in the pioneering work dedicated to Cu and Mn nanometer-scale metallic clusters, the XANES part is sensitive to the size of the cluster (Greaves *et al.*, 1981). In fact, at least two physical phenomenon can affect the intensity of the white line: the cluster size, which can be considered as an intrinsic effect (density of state of a nanometer scale cluster is far from the bulk one), and a possible charge transfer between the cluster and the support, which can be considered as an extrinsic one (Bazin *et al.*, 1997*a*,*b*). Regarding the sensitivity of the XANES, it is worth underlining that only the variation for very small clusters containing a few atoms can be detected (Bazin & Rehr, 2003). For larger clusters, EXAFS (Jentys, 1999) as well as wide-angle X-ray scattering (Ingham, 2015) constitute elegant solutions even if EXAFS is unsensitive to polydispersity (Moonen *et al.*, 1995).

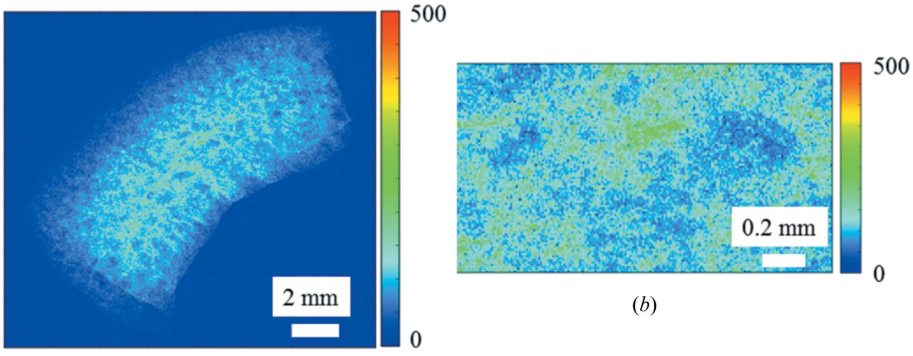

Figure 3
Large map (14 mm × 14 mm, 30 µm resolution, 30 ms acquisition time) (*a*) and map of region of interest (1900 µm × 960 µm, 10 µm resolution, 120 ms acquisition time) (*b*) for exposed rat based on the intensity of the X-ray fluorescence Au L_{α} emission showing the spatial distribution of QR-AuQDs particles in spleen.

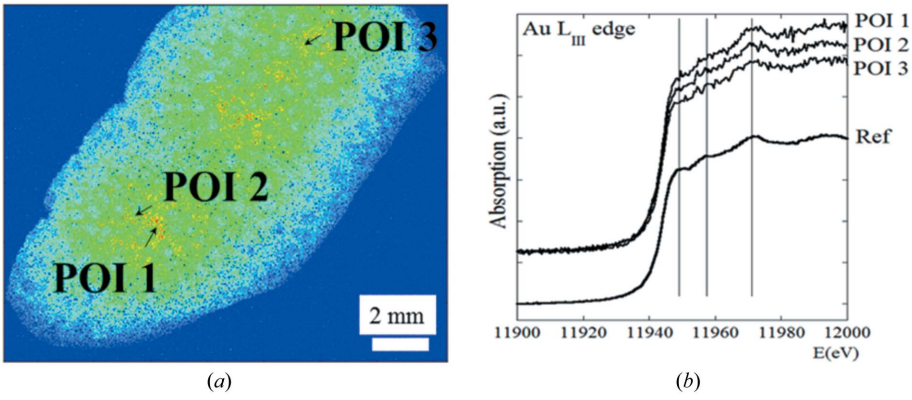

Figure 4
Map of Au *L*-fluorescence emission in spleen (15.6 mm × 16 mm, 30 µm resolution, 30 ms acquisition time) showing the different points of interest (POI1, POI2 and POI3) (*a*), and XANES spectra collected for each point of interest (*b*).

3. Results and discussion

Mesoporous silica nanomaterials are effective drug carriers, with large specific surface area and pore volume, favorable biocompatibility, and ease of functionalization *via* silane chemistry (Braun *et al.*, 2016; Xie *et al.*, 2016). Likewise, the progression to clinical trials of gold-based systems for photothermal therapy and drug/gene delivery advocates their potential for improving diverse treatments (Kunjachan *et al.*, 2015). Establishing their biodistribution and pharmacokinetics is a critical step towards their development in human pharmacology. Characterization techniques related to synchrotron radiation such as µXRF or µXAS have been extensively used in biology and medicine (Bazin *et al.*, 2006; Jackson *et al.*, 2009; Bohic *et al.*, 2012). Up to now, beam-time availability at synchrotron facilities was a serious limit to time-consuming point-by-point scanning techniques because biomedical experiments often require a large set of samples, combined with extensive areas of the sample to be imaged (several 10 mm^2). Flyscan continuous acquisition mode changes this paradigm.

Different characterization techniques such as X-ray fluorescence (Chen *et al.*, 2014; Jones *et al.*, 2016; Pérez *et al.*, 2016; Feng *et al.*, 2016), ptychography (Deng

et al., 2015; Huang *et al.*, 2015), scanning X-ray microscopy (McNulty *et al.*, 2003; Medjoubi *et al.*, 2013), scanning X-ray diffraction microscopy (Jones *et al.*, 2016; Li *et al.*, 2016) as well as fast differential phase-contrast imaging and total fluorescence yield mapping in a hard X-ray fluorescence microprobe (Vogt *et al.*, 2004) now use this experimental configuration. Thus, several breakthroughs have been performed in biological systems (Pushie *et al.*, 2014), and pathological calcifications (Bazin *et al.*, 2012) can be another research axis which can benefit from this experimental approach. These selected examples show that different Flyscan experimental setups exist. The SOLEIL Flyscan platform (described in §2.2) offers continuous scanning capabilities at high spatial resolution. Regarding our experiments, a single week of beam time allows us to detect and characterize our QR-AuQDs nanovector in 15 samples (three organs from five different rats).

The QR-AuQDs vector was detected in the spleen (Figs. 3 and 4), the liver [Figs. 5(*a*) and 5(*b*)] and in the kidney [Figs. 5(*c*) and 5(*d*)]. Au is not distributed homogeneously in the liver and spleen. The patchy distribution at a large (millimeter) lateral scale is confirmed by the high-resolution map. This indicates that the vector is likely to be partitioned into only some of the cells in those organs. These data are consistent with our finding using standard fluorescence microscopy and fluorescence using an isothiocyanate labeled vector (data not shown) where QR-AuQDs have been found accumulated in the reticuloendothelial system.

In the kidney, the contrast signal is more diffuse with enhancement in the cortex and at the cortico-medullary junction which is reminiscent of non-cellular specific deposits. It is noteworthy that the shapes of the obtained XANES spectra are not modified compared with those of the reference solution. This means that our vectors are stable under biological conditions at least for 4 h.

As seen in Fig. 2, one of the major strengths of µXRF is its ability to simultaneously acquire data on a large number of trace elements in the same acquisition. Here, the initial goal was to identify Au in the samples but information regarding the presence of Zn, Fe, Cu, Mn, Cr, Ti, V, Ca was also collected. These data were used to build a map of the spatial distribution of these different elements (Fig. 6).

At this point, it is essential to differentiate elements truly present in the kidney and elements present in the environment and the paraffin embedding the organ. Special attention has to be paid to the signal-to-background ratio in the maps, with the signal part being recorded in the organ and the background in the paraffin only. This organ/paraffin distinction can be easily seen from maps having high elemental contrast (*e.g.* Zn, Fe). Low-intensity signals, *i.e.* no contrast compared with the background part, should be disregarded. It is worth stressing that Ca, which has a significant presence in biological tissue, is associated with low fluorescence energy (Ca: K_α at 3691 eV, K_β at 4012 eV). Due to the air environment under our experimental conditions this fluorescence signal is highly absorbed, rendering any conclusion regarding Ca difficult.

Spatial redistribution itself can help to discriminate significant and spurious signals. Homogeneous distribution indicates that there is no enrichment within the biological sample and thus that these elements are from the paraffin. A statistical analysis (Fig. 7) can confirm the visual impression and give more precise information regarding the localization of all the elements identified in the X-ray fluorescence spectra. The fluorescence maps were analyzed using intensity correlation analysis methods in order to highlight possible correlations related to the presence of the elements in the tissue. For more details, the reader is referred to Li *et al.* (2004), Manders *et al.* (2003), Bolte & Cordelières (2006) and Estève *et al.* (2016*a*,*b*).

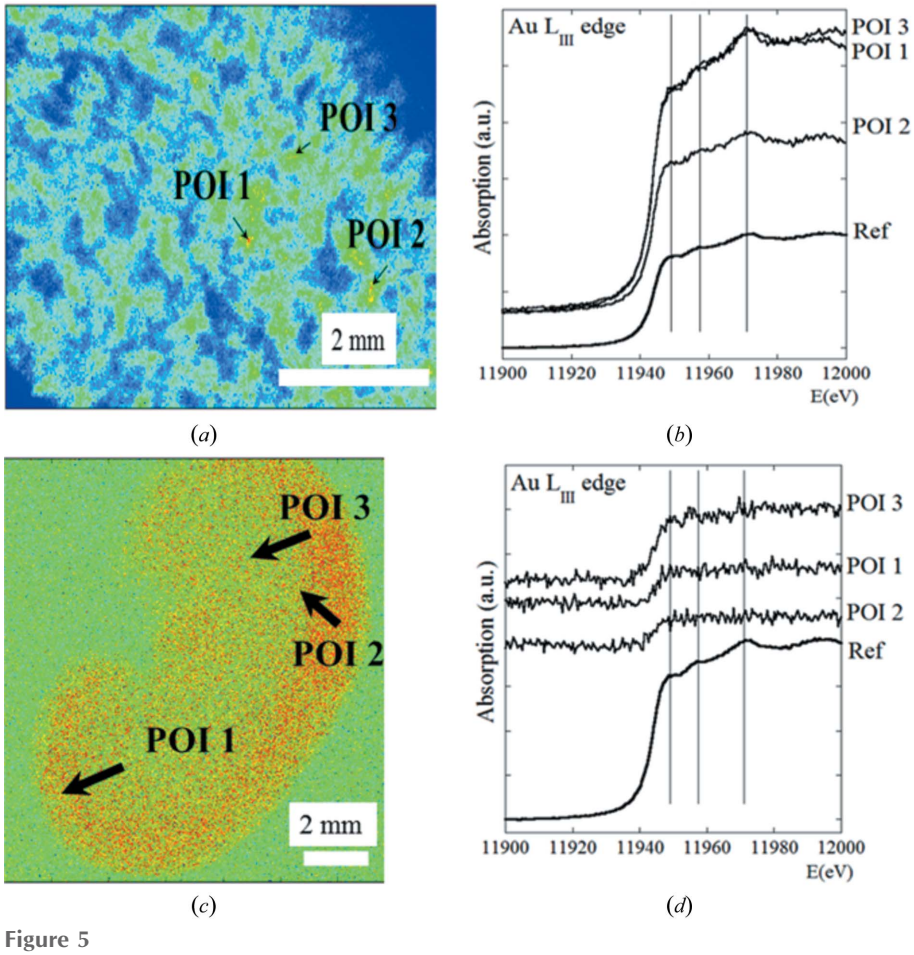

Figure 5
Maps built from the Au *L*-fluorescence emission showing the different points of interest (POI1, POI2 and POI3) selected (*a*) on liver (7 mm × 4 mm, 10 µm resolution) and (*c*) on kidney (15.5 µm × 14.4 mm, 30 µm resolution), and (*b*, *d*) XANES spectra collected for each respective point.

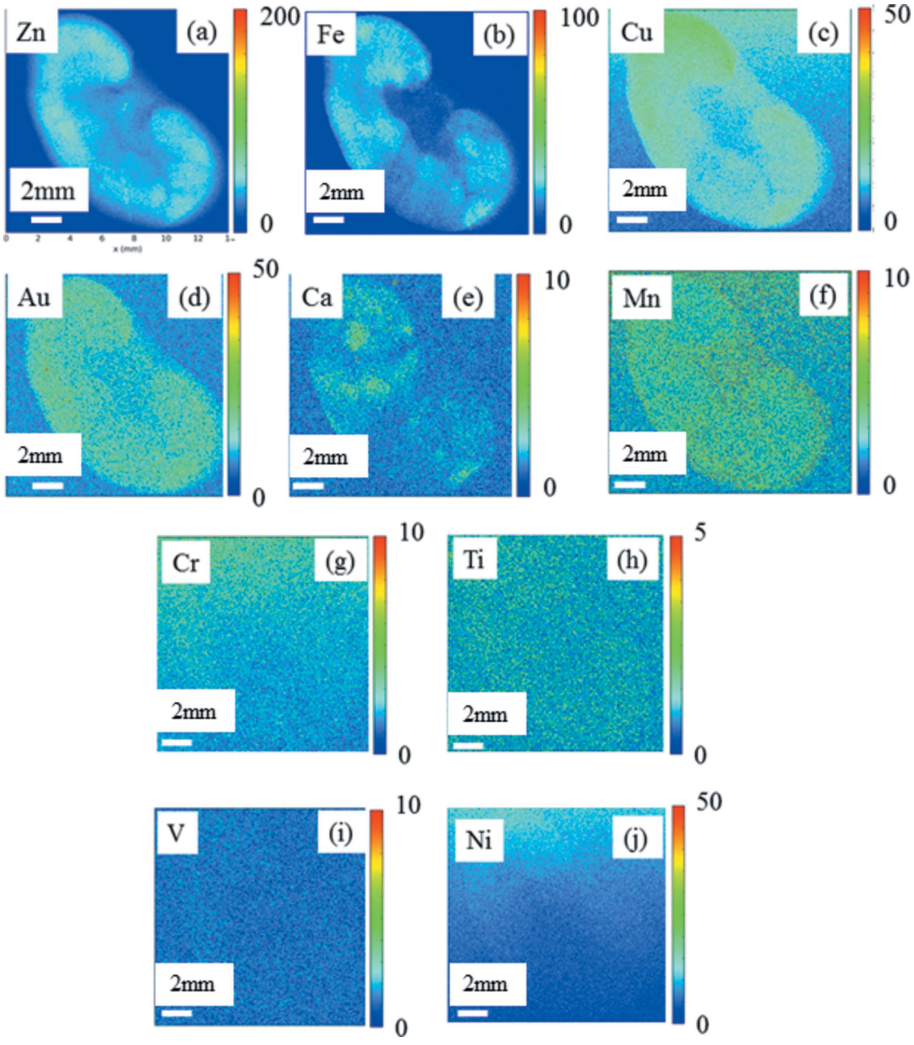

Figure 6
Spatial repartition of different elements, namely Zn (*a*), Fe (*b*), Cu (*c*), Au (*d*), Ca (*e*), Mn (*f*), Cr (*g*), Ti (*h*), V (*i*) and Ni (*j*), obtained using the intensity of the corresponding X-ray fluorescence emission lines (QR-AuQDs exposed rat kidney embedded in paraffin) as contrast (map 13.7 mm × 19.3 mm, 30 µm resolution, 20 ms acquisition time).

Such analysis shows that the main trace elements Fe, Zn and Cu are spatially correlated and do therefore correspond to the kidney. Correlation is much lower for Au and Mn but they should still be considered. The Ti and Cr fluorescence signals are very small, and the corresponding XRF maps show very low contrast scarcely above noise, with low and probably not significant correlation coefficients. Although Ni seems to be present in significant amounts (Fig. 2), there is a uniform XRF signal over the entire raster map with no contrast between the sample and its surroundings (Fig. 6*j*). This visual impression is confirmed by low correlation coefficients proving that, while Ni is abundant in the paraffin embedding material, it is insignificant in the organ in our sample.

In this investigation, special attention has been paid to possible spatial correlation between Zn and Au. Zinc was established as an essential trace element in 1961 (Prasad *et al.*, 1961). This element is an integral component of proteins involved in cell structure, and cell membrane stabilization. As reported recently (Foster & Samman, 2012), the extensive involvement of Zn in the immune system includes influencing the production and signaling of numerous inflammatory cytokines in a variety of cell types.

Several publications have assessed the relationship between Zn and

	Zn	Fe	Mn	Cu	Ca	Au	Ti	Cr	Ni
Zn		0.51	0.04	0.34	0.12	0.18	0.05	0.00	-0.04
Fe			0.12	0.32	0.21	0.13	0.07	0.04	-0.07
Mn				0.08	0.03	-0.10	0.00	0.03	-0.02
Cu					0.11	0.14	0.07	0.14	0.28
Ca						0.02	0.04	0.03	0.01
Au							0.03	0.01	0.01
Ti								0.04	-0.11
Cr									0.16
Ni									

	Zn	Fe	Mn	Cu	Ca	Au	Ti	Cr	Ni
Zn		0.72	0.44	0.67	0.51	0.55	0.46	0.46	0.46
Fe	0.74		0.52	0.68	0.59	0.55	0.49	0.48	0.41
Mn	0.46	0.46		0.49	0.45	0.41	0.44	0.48	0.45
Cu	0.62	0.55	0.46		0.49	0.54	0.47	0.53	0.62
Ca	0.52	0.50	0.41	0.53		0.49	0.47	0.47	0.46
Au	0.54	0.45	0.32	0.52	0.45		0.45	0.45	0.45
Ti	0.48	0.42	0.38	0.50	0.46	0.49		0.47	0.39
Cr	0.44	0.39	0.40	0.54	0.45	0.47	0.46		0.55
Ni	0.40	0.31	0.38	0.62	0.44	0.46	0.39	0.54	

Figure 7
Pearson (left panel) and Manders (right panel) coefficients calculated for all the possible combinations of XRF elemental maps. Red and blue correspond to positive and negative values, respectively; the darker the color, the larger are the absolute values. Note that the M1 and M2 coefficients (correlations between A–B and B–A elements, respectively, with A identified by the labels in the left-hand column and B the labels on the top line) appear in the right-hand panel. This is unnecessary for the Pearson correlation values, since the results are not sensitive to pairing order.

inflammation (Foster & Samman, 2012; Prasad, 2009; Bao *et al.*, 2008); it was already noted that Zn participates in regulating the physiological anti-inflammatory response (Dessombz *et al.*, 2013). To assess this, data on the spatial repartition of QR-AuQDs particles are presented (based on the intensity of the X-ray fluorescence Au L_α) and Zn (Zn K_α emission) for the rat kidney [Figs. 8(*a*) and 8(*b*)], spleen [Figs. 8(*c*) and 8(*d*)] and liver [Figs. 8(*e*) and 8(*f*)].

It is worth emphasizing that in kidney [Figs. 8(*a*) and 8(*b*)] Zn and Au signals are diffuse and co-localize in the cortex whereas in the spleen [Figs. 7(*c*) and 7(*d*)] and liver [Figs. 8(*e*) and 8(*f*)] the two signals differ. Spatial distribution data inform us that most of the vectors are trapped in specific compartments in the spleen and liver and only a few are non-specifically distributed in the kidney cortex; the Au signal is patchy whereas that from Zn is diffuse and homogeneous. This difference can be quantified statistically (Estève *et al.*, 2016*a*,*b*). The presence of QR in the tissue does not seem to be related to the inflammatory process (Fig. 8). The Pearson (Fig. 9, right panel) and Manders (Fig. 9, left panel) coefficients are both 0.7, and not close to 1, which would correspond to high Zn–Au correlation and a strong correlation of Au distribution with inflammation, as was the case for cisplatin (Estève *et al.*, 2016*a*,*b*), an anti-cancer drug associated with significant nephrotoxicity. This result is consistent with the literature showing that silica generated through soft chemistry does not provoke an inflammatory response.

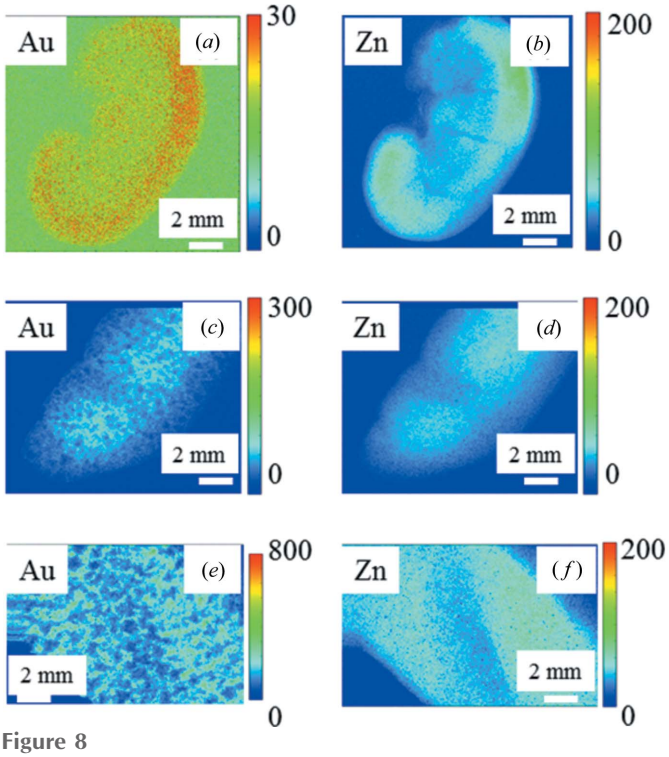

Figure 8
Spatial repartition of QR-AuQDs particles and Zn based on the intensity of the X-ray fluorescence Au L_α and Zn K_α emission for the various rat organs: kidney [panels (*a*) and (*b*)], spleen [panels (*c*) and (*d*)] and liver [panels (*e*) and (*f*)].

Finally, the potential of this approach in metal intoxication screening has to be emphasized. The kidney is directly involved in metal detoxification, with most heavy metals being sequestered by metallothionein proteins that are filtered and excreted by the kidney. Thus, several metals such as Pb, Hg, Cd, Cr, W and Cu (present as a result of intoxication or dysmetabolism) can lead to kidney failure through diverse mechanisms including redox damage after kidney accumulation (Barbier *et al.*, 2005; Reyes *et al.*, 2013). For example, μXRF data can help the clinician to establish a definite diagnosis of Wilson's disease (Kaščáková *et al.*, 2016). This rapid and versatile technique can be easily implemented in a clinical setting (Rouzière *et al.*, 2016), and applied to other heavy-metal pathologies such as saturnism (Pb) or hemochromatosis (Fe). Note that heavy elements related to metabolism such as iodine can be also the subject of similar analyses.

The Flyscan approach offers the ability to screen all these elements during the acquisition of 1 μm lateral resolution maps over a substantial number of samples, paving the way to a new pharmacotoxicologic approach for different organs. In comparison with standard inductively coupled plasma mass spectrometry, μXRF and μXAS determinations using the Flyscan geometry are nondestructive and provide spatial information.

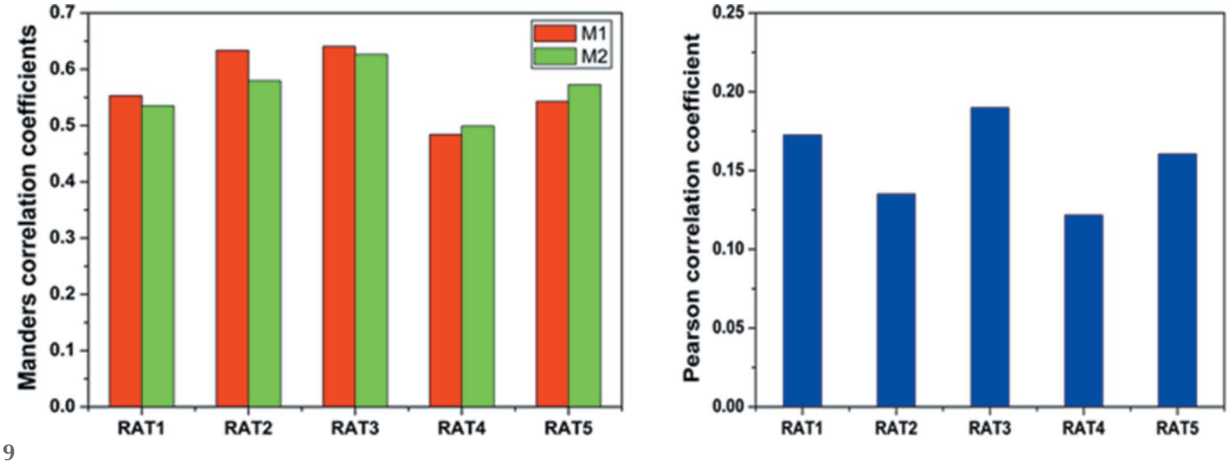

Figure 9
Pearson (right panel) and Manders (left panel) coefficients for Au and Zn for the kidneys of all the animals used in this study.

Furthermore, once detected, an element of interest can be explored in more detail using EXAFS and XANES, allowing a precise determination of the electronic state and atom environments. For some elements, it is of primary importance to determine their electronic state. For example, Cr^{3+} is considered to be an essential non-toxic micro-element required for proper human carbohydrate and fat metabolism. On the contrary, Cr^{6+} provokes severe toxic effects (Banerjee *et al.*, 2017).

4. Conclusion

The *in vivo* distribution and metabolism of 'quantum rattles' based on AuQDs confined in mesoporous silica has been investigated through µXRF and µXAS on a large number of samples, for the first time. The first technique yields the spatial distribution of QR-AuQDs in various rat organs, while the second indicates the stability of AuQDs. In only five days of experiment the Flyscan approach has yielded detailed information from three organs, *i.e.* kidney, liver and spleen, from five animals, paving the way for acquisition of novel clinically significant physicochemical data.

Acknowledgements

This work was supported by the Physics and Chemistry Institutes of CNRS (Centre National de la Recherche Scientifique). The authors are grateful to the SOLEIL (Source Optimisée de Lumière d'Energie Intermédiaire du LURE, Laboratoire pour l'Utilization du Rayonnement Electromagnétique) synchrotron facility for beam time allocation and would like to thank the support group of SOLEIL for their help during the experiment. JFG acknowledges the Karlsruhe Nano Micro Facility (KNMF).

References

Banerjee, S., Joshi, S. R., Mandal, T. & Halder, G. (2017). *Chemosphere*, **167**, 269–281.
Bao, B., Prasad, A. S., Beck, F. W., Snell, D., Suneja, A., Sarkar, F. H., Doshi, N., Fitzgerald, J. T. & Swerdlow, P. (2008). *Transl. Res.* **152**, 67–80.
Barbier, O., Jacquillet, G., Tauc, M., Cougnon, M. & Poujeol, P. (2005). *Nephron Physiol.* **99**, 105–110.
Bazin, D., Daudon, M., Chappard, C., Rehr, J. J., Thiaudière, D. & Reguer, S. (2011). *J. Synchrotron Rad.* **18**, 912–918.
Bazin, D., Daudon, M., Chevallier, P., Rouzière, S., Elkaim, E., Thiaudière, D., Fayard, B., Foy, E., Albouy, P. A., André, G., Matzen, G. & Véron, E. (2006). *Ann. Biol. Clin.* **64**, 125–139.
Bazin, D., Daudon, M., Combes, Ch. & Rey, Ch. (2012). *Chem. Rev.* **112**, 5092–5120.
Bazin, D. & Rehr, J. J. (2003). *J. Phys. Chem. B*, **107**, 12398–12402.
Bazin, D., Sayers, D. & Rehr, J. J. (1997*a*). *J. Phys. Chem. B*, **101**, 11040–11050.
Bazin, D., Sayers, D., Rehr, J. J. & Mottet, C. (1997*b*). *J. Phys. Chem. B*, **101**, 5332–5336.
Bohic, S., Cotte, M., Salomé, M., Fayard, B., Kuehbacher, M., Cloetens, P., Martinez-Criado, G., Tucoulou, R. & Susini, J. (2012). *J. Struct. Biol.* **177**, 248–258.
Bolte, S. & CordelièRes, F. P. (2006). *J. Microsc.* **224**, 213–232.
Braun, K., Pochert, A., Lindén, M., Davoudi, M., Schmidtchen, A., Nordström, R. & Malmsten, M. (2016). *J. Colloid Interface Sci.* **475**, 161–170.
Carpentier, X., Bazin, D., Jungers, P., Reguer, S., Thiaudière, D. & Daudon, M. (2010). *J. Synchrotron Rad.* **17**, 374–379.
Chen, S., Deng, J., Yuan, Y., Flachenecker, C., Mak, R., Hornberger, B., Jin, Q., Shu, D., Lai, B., Maser, J., Roehrig, C., Paunesku, T., Gleber, S. C., Vine, D. J., Finney, L., VonOsinski, J., Bolbat, M., Spink, I., Chen, Z., Steele, J., Trapp, D., Irwin, J., Feser, M., Snyder, E., Brister, K., Jacobsen, C., Woloschak, G. & Vogt, S. (2014). *J. Synchrotron Rad.* **21**, 66–75.
Deng, J., Nashed, Y. S. G., Chen, S., Phillips, N. W., Peterka, T., Ross, R., Vogt, S., Jacobsen, Ch. & Vine, D. J. (2015). *Opt. Express*, **23**, 5438–5451.
Dessombz, A., Nguyen, Ch., Ea, H. K., Rouzière, S., Foy, E., Hannouche, D., Réguer, S., Picca, F. E., Thiaudière, D., Lioté, F., Daudon, M. & Bazin, D. (2013). *J. Trace Elem. Med. Biol.* **27**, 326–333.
Estève, E., Bazin, D., Jouanneau, C., Rouzière, S., Bataille, A., Kellum, A., Provost, K., Mocuta, C., Reguer, S., Jorissen, K., Rehr, J. J., Hertig, A., Rondeau, E., Letavernier, E., Haymann, J. P., Daudon, M. & Ronco, P. (2016*a*). *C. R. Chim.* **19**, 1586–1589.
Estève, E., Bazin, D., Jouanneau, C., Rouzière, S., Bataille, A., Kellum, A., Provost, K., Mocuta, C., Reguer, S., Thiaudière, D., Jorissen, K., Rehr, J. J., Hertig, A., Rondeau, E., Letavernier, E., Daudon, M. & Ronco, P. (2016*b*). *C. R. Chim.* **19**, 1580–1585.
Feng, H., Qian, Y., Cochran, J. K., Zhu, Q., Hu, W., Yan, H., Li, L., Huang, X., Chu, Y. S., Liu, H., Yoo, S. & Liu, C. J. (2016). *Sci. Rep.* **7**, 40420.
Foster, M. & Samman, S. (2012). *Nutrients*, **4**, 676–694.
Greaves, G. N., Durham, P. J., Diakun, G. & Quinn, P. (1981). *Nature (London)*, **294**, 139–142.
Hembury, M., Chiappini, C., Bertazzo, S., Kalber, T., Drisko, G. L., Ogunlade, O., Walker-Samuel, S., Krishna, S. K., Jumeaux, C., Beard, P., Kumar, C. S. S. R., Porter, A. E., Lythgoe, M. F., Boissière, C., Sanchez, C. & Stevens, M. M. (2015). *Proc. Natl Acad. Sci. USA*, **112**, 1959–1964.
Huang, X., Lauer, K., Clark, J. N., Xu, W., Nazaretski, E., Harder, R., Robinson, I. K. & Chu, Y. S. (2015). *Sci. Rep.* **5**, 9074.
Ingham, I. (2015). *Crystallogr. Rev.* **21**, 229–303.
Jackson, B. P., Pace, H. E., Lanzirotti, A., Smith, R. & Ranville, J. F. (2009). *Anal. Bioanal. Chem.* **394**, 911–917.
Jain, P. K., Huang, X., El-Sayed, I. H. & El-Sayed, M. A. (2008). *Acc. Chem. Res.* **41**, 1578–1586.
Jentys, A. (1999). *Phys. Chem. Chem. Phys.* **1**, 4059–4063.
Jones, M. W. M., Phillips, N. W., van Riessen, G. A., Abbey, B., Vine, D. J., Nashed, Y. S. G., Mudie, S. T., Afshar, N., Kirkham, R., Chen, B., Balaur, E. & de Jonge, M. D. (2016). *J. Synchrotron Rad.* **23**, 1151–1157.
Kaščáková, S., Kewish, C. M., Rouzière, S., Schmitt, F., Sobesky, R., Poupon, J., Sandt, Ch., Francou, B., Somogyi, A., Samuel, D., Jacquemin, E., Dubart-Kupperschmitt, A., Nguyen, T. H., Bazin, D., Duclos-Vallée, J. C., Guettier, C. & Le Naour, F. (2016). *J. Pathol. Clin. Res.* **2**, 175–186.
Kirkpatrick, P. & Baez, A. V. (1948). *J. Opt. Soc. Am.* **38**, 766–774.
Kunjachan, S., Ehling, J., Storm, G., Kiessling, F. & Lammers, T. (2015). *Chem. Rev.* **115**, 10907–10937.
Lavenn, C., Albrieux, F., Bergeret, G., Chiriac, R., Delichère, P., Tuela, A. & Demessence, A. (2012). *Nanoscale*, **4**, 7334–7337.
Leclercq, N., Berthault, J., Langlois, F., Le, S., Poirier, S., Bisou, J., Blache, F., Medjoubi, K., Mocuta, C. (2015). *15th International Conference on Accelerator and Large Experimental Physics Control Systems (ICALEPCS'2015)*, Melbourne, Australia.
Li, C., Kiss, A. M., Van Campen, D. G., Garachtchenko, A., Kolotovsky, Y., Stone, K., Xu, Y., Zhang, W. & Corbett, J. (2016). *J. Synchrotron Rad.* **23**, 909–918.
Li, Q., Lau, A., Morris, T. J., Guo, L., Fordyce, C. B. & Stanley, E. F. (2004). *J. Neurosci.* **24**, 4070–4081.

McNulty, I., Paterson, D., Arko, J., Erdmann, M. S. P., Frigo, S. P., Goetze, K., Ilinski, P., Krapf, N., Mooney, T., Retch, C. C., Stampfl, A. P. J., Vogt, S., Wang, Y. & Xu, S. (2003). *J. Phys. IV Fr.* **104**, 11–15.
Manders, E. E. M., Verbeek, F. J. & Aten, J. A. (2003). *J. Microsc.* **169**, 375–382.
Medjoubi, K., Leclercq, N., Langlois, F., Buteau, A., Lé, S., Poirier, S., Mercère, P., Sforna, M. C., Kewish, C. M. & Somogyi, A. (2013). *J. Synchrotron Rad.* **20**, 293–299.
Min, Y., Caster, J. M., Eblan, M. J. & Wang, A. Z. (2015). *Chem. Rev.* **115**, 11147–11190.
Mocuta, C., Richard, M.-I., Fouet, J., Stanescu, S., Barbier, A., Guichet, C., Thomas, O., Hustache, S., Zozulya, A. V. & Thiaudière, D. (2014). *J. Appl. Cryst.* **47**, 482.
Moonen, J., Slot, J., Lefferts, L., Bazin, D. & Dexpert, H. (1995). *Physica B*, **208–209**, 689–690.
Nguyen, C., Ea, H. K., Thiaudiere, D., Reguer, S., Hannouche, D., Daudon, M., Lioté, F. & Bazin, D. (2011). *J. Synchrotron Rad.* **18**, 475–480.
Nguyen, K. T. & Zhao, Y. (2015). *Acc. Chem. Res.* **48**, 3016–3025.
Pérez, C. A., Murari, J. F. J., Moreno, G. B. Z. L., da Silva, J. L. & Piton, J. R. (2016). *AIP Conf. Proc.* **1764**, 030001.
Prasad, A. S. (2009). *Curr. Opin. Clin. Nutr. Metab. Care*, **12**, 646–652.
Prasad, A. S., Halsted, J. A. & Nadimi, M. (1961). *Am. J. Med.* **31**, 532–546.
Pushie, M. J., Pickering, I. J., Korbas, M., Hackett, M. J. & George, G. N. (2014). *Chem. Rev.* **114**, 8499–8541.
Reguer, S., Mocuta, C., Thiaudière, D., Daudon, M. & Bazin, D. (2016). *C. R. Chim.* **19**, 1424–1431.
Reyes, J. L., Molina-Jijón, E., Rodríguez-Muñoz, R., Bautista-García, P., Debray-García, Y. & Namorado, M. del C. (2013). *Biomed Res. Intl*, **2013**, 730789.
Rouzière, S., Bazin, D. & Daudon, M. (2016). *C. R. Chim.* **19**, 1404–1415.
Sayers, D. E., Stern, E. A. & Lytle, F. W. (1971). *Phys. Rev. Lett.* **27**, 1204–1207.
Shang, L., Dong, S. & Nienhaus, G. U. (2011). *Nano Today*, **6**, 401–418.
Slowing, I. I., Trewyn, B. G., Giri, S. & Lin, V. S.-Y. (2007). *Adv. Funct. Mater.* **17**, 1225–1236.
Solé, V. A., Papillon, E., Cotte, M., Walter, Ph. & Susini, J. (2007). *At. Spectrosc.* **62**, 63–68.
Song, Z., Kenney, J. P. L., Fein, J. B. & Bunker, B. A. (2012). *Geochim. Cosmochim. Acta*, **86**, 103–117.
Stöber, W., Fink, A. & Bohn, E. (1968). *J. Colloid Interface Sci.* **26**, 62–69.
Vogt, S., Feser, M., Legnini, D., Kirz, J. & Maser, J. (2004). *AIP Conf. Proc.* **705**, 1348–1351.
Xie, J., Xiao, D., Zhao, J., Hu, N., Bao, Q., Jiang, L. & Yu, L. (2016). *Adv. Healthc. Mater.* **5**, 1213–1221.
Yang, X., Yang, M., Pang, B., Vara, M. & Xia, Y. (2015). *Chem. Rev.* **115**, 10410–10488.
Yuan, Z., Pan, Y., Cheng, R., Sheng, L., Wu, W., Pan, G., Feng, Q. & Cui, W. (2016). *Nanotechnology*, **27**, 245101.